Role of threading dislocations on the growth of HgCdTe epilayers investigated using monochromatic X-ray Bragg diffraction imaging

Can Yildirim,[a,b]* Philippe Ballet,[a] Jean-Louis Santailler,[a] Dominique Giotta,[a] Rémy Obrecht,[a] Thu Nhi Tran Thi,[b] José Baruchel[b] and Delphine Brellier[a]

[a]Universite Grenoble Alpes, CEA, 17 Avenue de Martyrs, 38000 Grenoble, France, and [b]European Synchrotron Radiation Facility, 74 Avenue de Martyrs, 38000 Grenoble, France. *Correspondence e-mail: can.yildirim@esrf.fr

High-quality $Hg_{1-x}Cd_xTe$ (MCT) single crystals are essential for two-dimensional infrared detector arrays. Crystal quality plays an important role on the performance of these devices. Here, the dislocations present at the interface of CdZnTe (CZT) substrates and liquid-phase epitaxy grown MCT epilayers are investigated using X-ray Bragg diffraction imaging (XBDI). The diffraction contributions coming from the threading dislocations (TDs) of the CZT substrate and the MCT epilayers are separated using weak-beam conditions in projection topographs. The results clearly suggest that the lattice parameter of the growing MCT epilayer is, at the growth inception, very close to that of the CZT substrate and gradually departs from the substrate's lattice parameter as the growth advances. Moreover, the relative growth velocity of the MCT epilayer around the TDs is found to be faster by a factor of two to four compared with the matrix. In addition, a fast alternative method to the conventional characterization methods for probing crystals with low dislocation density such as atomic force microscopy and optical interferometry is introduced. A 1.5 mm × 1.5 mm area map of the epilayer defects with sub-micrometre spatial resolution is generated, using section XBDI, by blocking the diffraction contribution of the substrate and scanning the sample spatially.

1. Introduction

$Hg_{1-x}Cd_xTe$ (MCT) crystalline epilayers have been the workhorse for high-performance infrared detectors. The crystalline perfection of these epilayers is of great importance, as defects or variations of local composition can result in performance degradation of the MCT-based detector.

One of the main reasons for these types of degradation is the presence of dislocations, which can be threading and/or misfit dislocations. Threading dislocations can originate from the substrate (emerging dislocations or due to surface preparation) or can be generated in association with stresses occurring during the growth process. On the other hand, misfit dislocations can arise between the substrate and the epilayer when the epilayer thickness exceeds a 'critical thickness', to relax the elastic energy associated with the lattice mismatch at the interface (Matthews & Blakeslee, 1974). There is another way of relaxing this elastic energy, that is if the epilayer during its growth, is able to exhibit a composition (and therefore lattice parameter) variation (Marichev et al., 2018).

$Cd_{1-y}Zn_yTe$ (CZT) has been the most widely used substrate for MCT growth as it offers remarkably small amounts of lattice mismatch ($\sim 10^{-4}$) with the MCT epilayer (Basson & Booyens, 1983; Takigawa et al., 1988). Nevertheless, in our earlier studies we observed misfit dislocations (see the

HgCdTe Layer

Emerging spirals   Threading Dislocations

CdZnTe Substrate
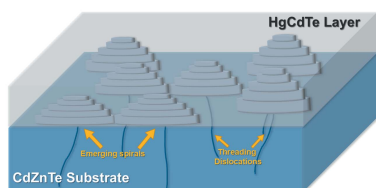
supporting information) which can have an impact on the different processing steps in the device fabrication resulting in failure. Careful production and keeping the epilayer below the critical thickness for misfit dislocations help to eliminate these types of defects. However, even in this case, the epilayers exhibit defects and compositional inhomogeneity. The characterization of these defects is of great scientific and industrial importance.

Existing conventional characterization techniques for investigating defects in MCT–CZT systems are mostly destructive or indirect. One of the most widely used techniques for studying defects in CZT substrates or MCT epilayers is chemical etching. Typical etch-pit density studies can provide quantitative analysis on dislocation densities. However, this method is difficult to apply to interfaces due to the requirement of different etching agents for each material in question, and their dependence on the chemistry and crystallography (Everson *et al.*, 1995; Hähnert & Schenk, 1990). Furthermore, this method is destructive and the samples cannot be used for further fabrication steps.

Another method for investigating defects in MCT–CZT systems is to study the dislocation densities indirectly using the full width at half-maximum (FWHM) of a typical X-ray rocking curve. This technique is applicable for systems having dislocation densities high enough to be measured by the FWHM. Yet, the defect density resulting from this type of analysis does not provide decoupled analysis for the substrate and the layer, and/or for different dislocation types, *i.e.* misfit and threading dislocations, since the rocking curve includes contributions from both types of dislocations (Ayers, 1994; Fourreau *et al.*, 2016). Thus, it can be difficult to differentiate the origin of the epilayer defects with this technique.

The epilayer defects can be probed using atomic force microscopy (AFM) or interferometry (Fourreau *et al.*, 2016). These two methods complement each other in terms of lateral spatial and height resolution, and field of view, respectively. On the one hand, AFM has a better spatial resolution and height sensitivity yet it is time-consuming to probe larger areas compared with optical interferometry. Thus, in systems with low dislocation density, it is a challenge to study the epilayer defects as the probability of finding one is low due to the field of view. On the other hand, one can map a larger area rather quickly using optical interferometry, yet at the expense of the spatial resolution. Moreover, neither of these methods can be applied to study interfaces.
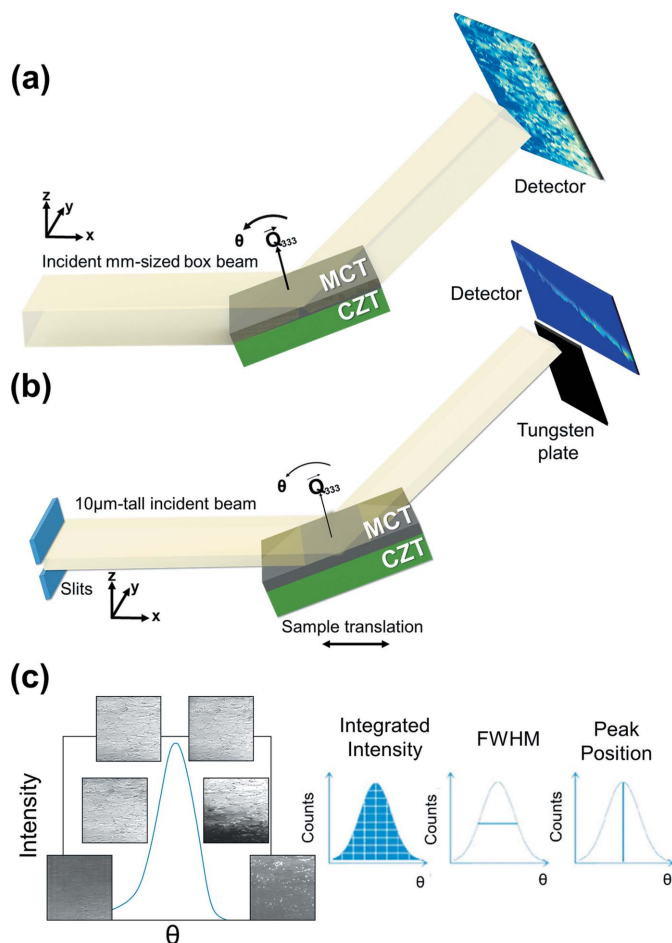
Transmission electron microscopy (TEM) can directly detect the spatial distribution of dislocations with real and reciprocal space information thanks to the adjustable objective lenses (Williams & Carter, 1996). However, the information obtained by TEM is limited to a small area thus it may not be representative of the entire sample. Moreover, in CZT–MCT systems the dislocation density is extremely low (10^3–10^4 cm^{-2}) to be detected by TEM. Similar to etch-pit studies, TEM is also a destructive method as the samples need to be cut into thin slices. Moreover, the sample preparation of TEM analyses are known to introduce dislocations to this material system.

None of the above-mentioned methods provide an optimal way of investigation of the layer–substrate interface that is needed to improve the understanding of the defects embedded in the 3D structure in a non-destructive manner. Therefore, there is a need for a non-destructive method that can probe not only the epilayer–substrate interface but also the epilayer itself in a representative manner combined with high angular resolution, that can probe the strain fields around defects. X-ray Bragg diffraction imaging (XBDI), historically known as X-ray diffraction topography, offers an interesting option for overcoming the above-mentioned difficulties. XBDI is a well established non-destructive imaging technique based on Bragg diffraction that provides image contrast from lattice strain and orientation. XBDI has been widely used to study crystal defects with sub-micrometre spatial and high angular resolution (microradians) (Bowen & Tanner, 1998; Authier, 2006; Lübbert *et al.*, 2000, 2005). By employing rocking curve imaging (RCI), which is the quantitative variant of X-ray monochromatic topography, one can study local distortions in a crystal due to lattice parameter variation and lattice tilt (Tran Thi *et al.*, 2017). These features make XBDI a powerful tool for non-destructive investigations of crystal defects.

In this work, we study the defects in MCT epilayers grown by liquid-phase epitaxy (LPE) on CZT substrates by means of XBDI using a synchrotron source. We present a fast, alternative method to AFM to characterize the structural defects of the MCT epilayer over millimetre-squared areas with micrometre resolution and diffraction contrast using section XBDI by blocking the diffraction contribution of the substrate. Furthermore, we employ a projection geometry RCI to investigate the origin of the epilayer defects and their correlation with the substrate defects. Our results show both qualitatively and quantitatively the link between substrate defects and epilayer distortions and their spatial distribution along with their effect on relative growth velocity.

2. Experimental

We conducted the XBDI experiments at the European Synchrotron Radiation Facility (ESRF) at beamline BM05. A double-crystal Si(111) monochromator was used to select a monochromatic X-ray beam having 15 keV photon energy. We utilized an ESRF-developed FReLoN CCD 2048 × 2048 pixel detector positioned 300 mm downstream of the sample. The optics coupled with the detector achieved an effective pixel size of 0.75 μm. We probed the 333 Bragg reflection of the sample at a Bragg angle of 19.7. All measurements were carried out in reflection geometry. Fig. 1(*a*) shows the experimental set up for rocking curve imaging using a 1.4 mm × 1.4 mm-sized beam. This part of the experiment was conducted by illuminating the whole area and distinguishing the substrate and layer images through their angular locations on the rocking curve. A total of 140 images were recorded with an angular step size of 10^{-4} degrees within an angular range of 0.014°. For the RCI data reconstruction we generated peak position, integrated intensity and FWHM maps as illustrated

To ensure that the CCD read only the epilayer contribution, the tungsten plate was mounted in such a way that it blocked the lower part of the diffracted signal in vertical geometry, because the epilayer diffraction reached the upper part of the CCD detector in the geometry we are concerned with. Subsequently the sample was spatially scanned along the beam axis in such a way that a small overlap was achieved between the section diffraction images of two consecutive locations on the epilayer. This procedure facilitated the data reconstruction.

We studied samples with MCT epilayers grown by liquid-phase epitaxy (LPE) (Pelliciari, 1994) on vertical gradient freeze (VGF) bulk (111)-oriented CZT. Several factors affect the crystal quality of MCT epilayers. Of special importance, the crystal quality of the bulk CZT substrate has to be high, *i.e.* low defect and dislocation densities. We selected CZT substrates with dislocation densities in the range 10^3–10^4 cm^{-2} (Brellier *et al.*, 2014). Moreover, the surface has to be carefully prepared to avoid scratches and to remove polishing damage. A double-sided mechanical polishing combined with chemical-mechanical polishing (Pelenc *et al.*, 2014) was applied as a finishing step.

Controlling the substrate–epilayer lattice mismatch is another crucial step in synthesizing high-quality crystals. Lattice matching should be ensured to avoid strain relaxation, which may generate misfit dislocations in the epilayer. This can be achieved by optimizing the Zn fraction of the CZT substrate on which the MCT epilayer growth takes place. We pre-characterized some epilayers using XBDI to find the best lattice-matching conditions by avoiding the appearance of the misfit dislocations (see the supporting information). Therefore, for this work, we chose an MCT epilayer free of such crosshatch appearance. The selected MCT epilayer was grown in the ⟨111⟩ orientation with a cadmium fraction of about 0.29, targeting the detection in the middle wavelength infrared band. The final thickness of the MCT epilayer was about 7 μm. The epilayer studied was grown on a CZT substrate, the Zn fraction of which was carefully chosen in order to avoid any lattice mismatch between the epilayer and the substrate. Thus, the average lattice mismatch between CZT and MCT was estimated as ∼10^{-4} from the data obtained with a laboratory X-ray source.

Figure 1
Schematics of the rocking curve imaging (RCI) experiments. (*a*) Projection RCI with a millimetre-sized box beam illuminating the sample in reflection geometry. The 2D detector having 0.75 μm pixel size is positioned at 330 mm downstream of the sample. (*b*) Scanning section RCI with 10 μm-tall beam selected by the Au slits. The tungsten plate is placed close to the detector to block a part of the diffracted beam generated by the CZT substrate so that only the diffracted beam by MCT reaches the detector. The sample is translated along the beam, the *x* direction, as shown. (*c*) Reconstructed maps of integrated intensity, FWHM and peak position are generated using the rocking curve data.

in Fig. 1(*c*) (Tsoutsouva *et al.*, 2014). To generate this map, 140 2D images were stacked together, and a Gaussian fitting was performed to individual rocking curves at each pixel of the CCD detector. The details of the generation of this type of maps can be found elsewhere (Tran Thi *et al.*, 2017).

Fig. 1(*b*) illustrates the principles of a scanning section-topography experiment, inspired by the procedure described by Lang (1963) adapted to our experimental conditions. In particular, Lang's method was adapted to the requirements imposed by the nearly parallel synchrotron radiation beam we use. In this case, a 10 μm-tall beam was selected using Au slits to perform section XBDI experiments, and a tungsten plate was mounted on a motorized stage close to the detector (Lang, 1963) to block the diffracted beam associated with the substrate. The sample was translated along the beam axis to be able to cover a 1.08 mm × 1.5 mm area of the MCT epilayer.

3. Results

3.1. X-ray rocking curve imaging of CZT-MCT ensemble

We used projection RCI (Lübbert *et al.*, 2000) in reflection geometry to investigate the CZT-MCT defects. Fig. 2(*a*) shows the 333 Bragg reflection rocking curve. At this energy and diffraction geometry, the incident beam goes through the MCT epilayer at an incidence of 19.7° before it reaches the substrate. Thus, the diffracted signal from the substrate has to travel through the same thickness of MCT epilayer before it exits the epilayer. The X-ray attenuation length through MCT at 15 keV is ∼15 μm. As a result, the incident beam onto
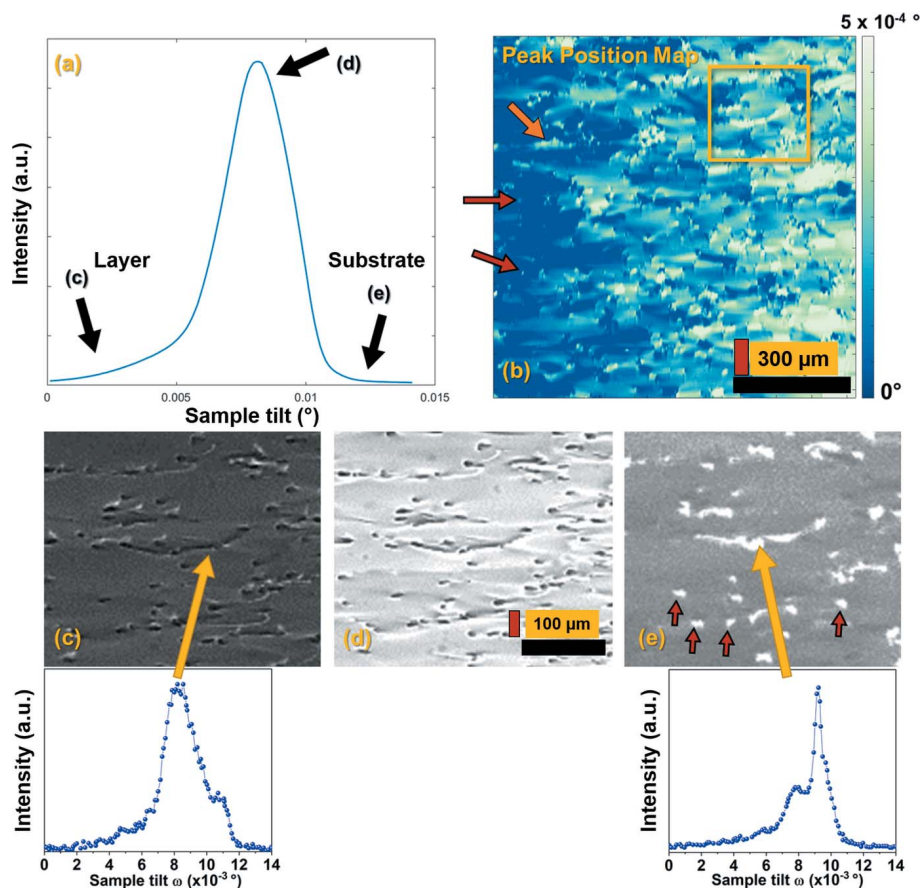
Figure 2
(*a*) Total rocking curve showing the contributions from the layer and the substrate. (*b*) Calculated peak position map at 15 keV for the 333 Bragg reflection. The field of view is 1.5 mm × 4.7 mm (horizontal × vertical). Raw X-ray topographs of (*c*) the weak-beam condition of the MCT layer, (*d*) at the peak position, (*e*) the diffracted image on the Bragg condition of the substrate. The yellow arrows show examples of the correlated defects whereas the red arrows show threading dislocations of the substrate. White color indicates higher intensity. All intensity values are shown in a linear scale. The red scale bars in (*b*) and (*d*) show the vertical length scale, 300 and 100 μm, respectively. The black scale bars represents the horizontal length scale.

the CZT and the diffracted beam from the CZT substrate is attenuated along ∼41 μm distance through the MCT epilayer, resulting in a 5% X-ray transmission. Consequently, the observed total rocking curve, which is the sum of all pixel intensities of each image (140 in total) at a given θ value, has a dominant contribution from the MCT epilayer and has only a small contribution from the CZT substrate. As for the CZT diffraction contribution to this rocking curve, exclusively, the regions with higher diffracted intensity from the substrate, *i.e.* dislocations, and only the regions close to the interface with the MCT epilayer should yield a detectable intensity. The expected angular position of the substrate is shown on the side of the epilayer–substrate rocking curve in Fig. 2(*a*).

Thus, the RCI maps produced from the images recorded along the rocking curve show, as a first approximation, features corresponding to the epilayer since the MCT diffraction dominates the total rocking curve. Fig. 2(*b*) shows the peak position map, (*i.e.* center of mass map) of the RCI. Fig. 2(*b*) shows that the peak positions of the different areas of the sample are spread over an angular range of 5×10^{-4} [scale

on the right side of the Fig. 2(*b*)]. Note that a weak curvature of the diffracting planes from the left to the right side of the area investigated (radius of curvature ∼200 m) is observed. The observed curvature has an angular value that is smaller than the FWHM of the Fig. 2(*a*) rocking curve (∼5×10^{-3}) because the peak position map is corrected for dispersion (Servidori *et al.*, 2001).

Let us remark on the presence of 'dot-like' regions in Fig. 2(*b*) (red arrows on the figure) displaying a higher peak position-value, which appears to be eminently close to the expected Bragg position of the substrate. These dot-like regions are often linked by lines that also exhibit higher peak-position values (orange arrow in the figure), in such a way that these 'dot-like' features, typically separated by 50–60 μm, are connected and form 'islands', as also seen as white areas in Fig. 2(*e*).

To obtain clues about the origin of these dot-like and island-like features we carefully analyzed some of the raw (*i.e.* unprocessed) images zoomed from the yellow-framed area shown in Fig. 2(*b*) at different points [indicated in Fig. 2(*a*)] along the measured rocking curve. The brighter parts indicate higher intensity. Images recorded on the tails of the rocking curve correspond to 'weak-beam' conditions, which are widely used to enhance the contrast of defects such as dislocations, notably in dark-field microscopy and XBDI (Cockayne *et al.*, 1969; Fung *et al.*, 1997; Jakobsen *et al.*, 2019; Sauvage *et al.*, 1980).

Let us start with Fig. 2(*e*), where dot-like features, sometimes connected, are visible. This figure, which shows the high θ weak-beam condition of the epilayer, is recorded at an angle with respect to the peak of the rocking curve which roughly corresponds to an angular departure compatible with the lattice parameter variation between the substrate and the epilayer. Thus, at this location we examined features that could correspond to the substrate contribution to the diffraction. The inset of Fig. 2(*e*) shows the rocking curve for one pixel of the detector that is pointed with the yellow arrow. This rocking curve corresponds, within a sensible first approximation, to a volume of ∼0.75 μm × 0.75 μm × 25 μm elongated along the diffraction direction. The 25 μm we suggest for the length of the voxel corresponds to the 21 μm of the epilayer when viewed along the diffracted direction, and to an estimated small thickness, ∼3–4 μm, originating from the substrate. The Bragg diffraction by this 'voxel' volume produces a rocking curve with two peaks. One of the

two peaks (the one corresponding to the higher θ) is particularly narrow ($\sim 6 \times 10^{-4}$). This indicates that the peak is associated with the high crystalline quality substrate. The narrow peak is not (or only faintly) observed when looking at the rocking curve of a pixel where dots-related-features are not present. This suggests that the dots correspond to highly diffracting regions of the substrate, whereas the substrate 'matrix' contribution is too low to produce an observable peak. The simplest interpretation of these narrow peak/highly diffracting regions of the substrate is that they are the images of emerging threading dislocations (TDs) of the substrate. Small red arrows point out some of these dislocations in Fig. 2(e). The density of the TDs calculated from the image is $\sim 1.5 \times 10^3$ cm^{-2}, which is in line with our previous work (Brellier et al., 2014). Moreover, one can see bright horizontal lines (i.e. islands) connecting the TDs (around the yellow arrow). We observe these connecting bright lines or 'islands' around the TDs, in the immediate angular neighborhood of the substrate Bragg position, and their intensity decreases when going towards the peak of the rocking curve. This indicates that they correspond to the parts of the MCT epilayer at high θ weak-beam condition that have a lattice parameter close to that of the substrate. Note that these islands are observed between dots in the peak position map, Fig. 2(b), as well.

Fig. 2(d) shows the raw image at the peak position of the rocking curve, where most of the intensity comes from the MCT epilayer matrix, since, as mentioned before, the diffraction contribution from the substrate is mostly absorbed through the MCT epilayer thickness. Fig. 2(d) shows that the bright regions observed in Fig. 2(e) are now darker than the matrix, whereas other dark or white regions are present. This contrast is associated with the regions satisfying (or not) the Bragg condition, without having to invoke other image contrast mechanisms such as direct or dynamical images (Authier, 2006). These image contrast mechanisms occur when the crystal matrix is highly perfect and that the thickness of this perfect crystal is bigger than about half of the extinction length (Tanner, 2013). The 7 µm-thick epilayer we are concerned with displays a thickness of the order of the extinction length (Λ = 8.6 µm in our case) and cannot be considered as a perfect crystal because, as will be discussed in the next paragraph, it displays a range of lattice parameters.

Fig. 2(c) shows a low θ weak-beam condition for the epilayer. The bright islands observed in Fig. 2(e), at the high θ part of the rocking curve, exhibit a lower diffracted intensity compared with the matrix in Fig. 2(c), which corresponds to the low θ part of the rocking curve. The FWHM of the rocking curve shown in the inset of Fig. 2(c), which corresponds to a pixel located outside the 'island' and therefore mainly to the epilayer contribution, is about four times wider than the 'substrate peak' of the inset of Fig. 2(e). This suggests that the corresponding voxel, again ~ 25 µm elongated along the diffracted direction, displays a range of lattice parameters, with an estimated $\Delta d/d \simeq 8 \times 10^{-5}$. We will elaborate on this in more detail in the Discussion section.

From the rocking curve images, one can extract the angular misorientation between the layer and the substrate. The local effective misorientation, $\Delta\theta$, is given as

$$\Delta\theta = \delta\theta + \frac{\Delta d}{d}\tan(\theta) \qquad (1)$$

where d is the d spacing, the $\delta\theta$ term is the lattice tilt contribution and $(\Delta d/d)\tan(\theta)$ is the contribution of the lattice parameter variation. In the plane of diffraction for this experiment, the dominant term is the latter, the lattice parameter variation. Thus the lattice parameter variation between the layer and the substrate can be calculated using the following equation,

$$\frac{\Delta d}{d} \simeq \frac{\Delta\theta}{\tan(\theta_{\text{Bragg}})} \qquad (2)$$

where d is the lattice plane spacing of a given reflection and θ is the Bragg angle. Utilizing this equation on the rocking curves of a number of individual pixels that show two separated peaks, the lattice parameter variation is calculated as $1.2 \pm 0.2 \times 10^{-4}$. Let us recall, as mentioned before, that not all the pixels show two peaks since the beam goes through an absorbing epilayer of MCT before it reaches the CZT substrate. Thus, the defect-free regions of the substrate do not yield a diffracted intensity high enough to become visible. Given these conditions, the reconstructed FWHM and peak position maps from the 'total' rocking curve can be misleading, and are not adequate tools to investigate the defects in our rather complicated sample. Nevertheless, relevant information can be extracted from reduced angular maps. In this respect, we treated the MCT and CZT contributions separately to produce a first map having a main contribution originating from the epilayer whereas the second one maximizes the contribution of the substrate.

Fig. 3 shows two calculated integrated intensity maps of the MCT epilayer and CZT substrate, generated by separating the contributions of the respective parts of the rocking curve (i.e. choosing 30 raw images from the low θ weak-beam condition of the epilayer and from the regions where the substrate is known to be in the Bragg condition). The total intensity maps [Fig. 3(a) and 3(b)] show different pictures. In Fig. 3(b) one can observe dots that can be the images of the TDs emerging
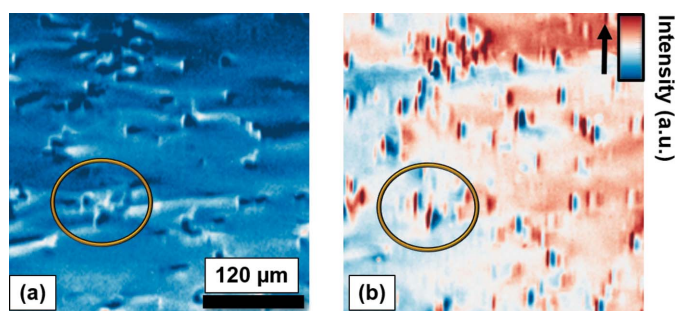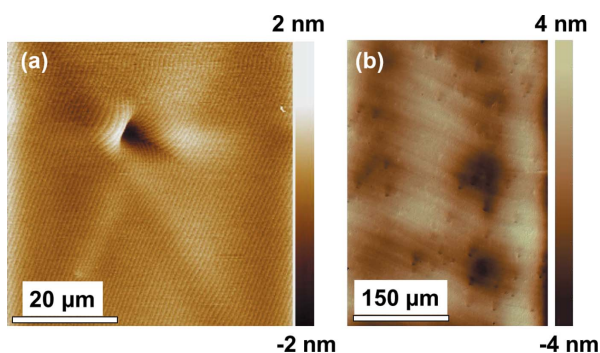

Figure 3
The integrated intensity maps for the (a) MCT epilayer and (b) CZT substrate. The intensity increases from blue to red color in arbitrary units. One example of the correlated defects are shown within the circles.

from the substrate. The contrast of these dots is sometimes complex, and could be related to the characteristics of the dislocations (Köhler, 1994; Möhling *et al.*, 1993). In Fig. 3(*a*), one can observe features associated with inhomogeneities within the epilayer, which correspond to the defects observed in Fig. 3(*b*). These images point out the correlation between the emerging dislocations in CZT and the MCT regions displaying contrast at the low θ integrated intensity map, and suggest that the substrate dislocations propagate within the epilayer. The golden-colored circle points out an example of these correlated defects in low and high θ weak-beam conditions for the MCT epilayer.

3.2. Section XBDI for mapping a large area of the MCT layer

Our aim is the characterization of large areas of the epilayer, which is of paramount importance for understanding the structure of defects and their distribution across a relevant distance. The images shown on Fig. 2(*c*)–2(*e*), albeit providing interesting information, result from calculations performed on a set of raw images. However, the selection of this set of images may not be obvious, and we cannot guarantee that the epilayer image is completely free from a substrate contribution. Therefore, this section is devoted to a technique that blocks this substrate contribution.

Firstly, let us revisit some of the existing, widely used surface characterization tools such as AFM and interferometry. Both methods provide important data, but have certain drawbacks. Fig. 4 shows the surface characterization of the sample after the synchrotron experiment using (*a*) AFM and (*b*) optical interferometry. Fig. 4(*a*) shows a $\sim$10 μm-sized surface defect, which could correspond to a dot-like defect observed in Fig. 2. We can observe the distortions around this defect through the image of the growth atomic steps, thanks to the spatial resolution given by AFM. However, with the limited field of view of AFM, the chances of falling onto such defects are limited. Fig. 4(*b*) reveals a large field of view interferometry map of the same epilayer. Some dot-like defects are visible across the map. Yet, even though this map helps identify defects in a statistical manner, due to the limitations in resolution, one cannot extract detailed structural analysis.
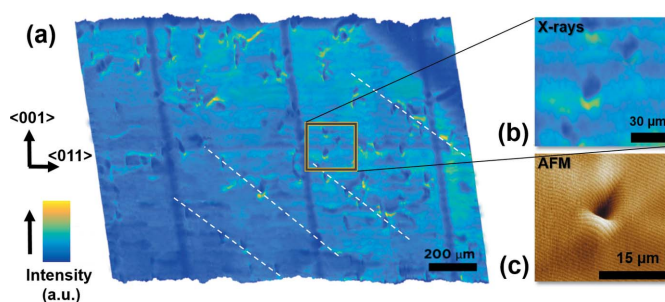
Figure 5
(*a*) Ensemble of the stitched epilayers of 10 μm raw images located at the peak position of the rocking curve from the section topographs of the MCT epilayer. The whited dashed lines emphasize the alignment of the defects. Three observed dark, vertical lines are artifacts coming from the slits. Bright colors show higher intensity. (*b*) XBDI and (*c*) AFM comparison of a similar defect.

To overcome this problem, we adapted a method suggested half a century ago to the synchrotron radiation environment (Lang, 1963), with an approach that incorporates scanning of the sample using section XBDI.

Fig. 5(*a*) shows the reconstructed map from the section XBDI experiment. The section topographs at each scanning point are stitched to form a total map that covers 1.1 mm × 1.5 mm area. At a first glance to Fig. 5(*a*), one can see void-like features of about 20 μm distributed with a number density of $\sim$7 × 10^2 cm^{-2}, which corresponds well to the number density of TDs of the CZT substrate [extracted from Fig. 4(*b*)]. An interesting point about these void-like features is that they have a lower diffracted intensity compared with the matrix. This corresponds to the fact that the main contrast mechanism originates from regions satisfying, or not, the Bragg condition. Our procedure is such that we record, for each slice (*i.e.* section), an image that corresponds to the peak of the rocking curve of the epilayer, *i.e.* the epilayer matrix. The neighborhood of the defects, distorted with respect to the MCT matrix, displays a Bragg position different from that of the MCT matrix, and appear less illuminated in the image we recorded. Most of these defects tend to group together. Some of them show an intensity increase around one of their borders (*i.e.* yellow color). A closer look at Fig. 5(*b*) shows that these epilayer defects are aligned in such a way that they make about 60° with ⟨110⟩ and are orthogonal to ⟨111⟩ directions, indicating the most densely packed directions. Overall, this method provides a fast and non-destructive option for studying the structural defects of large areas with diffraction contrast.

4. Discussion

The scanning section XBDI results [Fig. 5(*a*)] of the MCT epilayer showed void-like defects on a large area of the epilayer, which cannot be probed using AFM nor interferometry at reasonable timescales. Our RCI results showed a correlation between these void-like defects and the TDs of the CZT substrate [Fig. 2(*e*)]. It is therefore highly probable that the substrate defects affect the epilayer quality and topology.

Figure 4
(*a*) Atomic force microscopy and (*b*) interferometry images of the MCT layer. The color map shows the topological differences of the surface.

Our discussion will show that the defects of the substrate locally modify the epilayer growth conditions. Fig. 2 shows 'islands' that are produced around the locations of the emerging dislocations of the substrate, located at the high-θ side of the rocking curve [Figs. 2(b) and 2(e)]. Dislocations can create energetically favorable sites for crystal growth (Frank, 1949; Quéré, 1998). This suggests a dislocation-promoted growth, as we will discuss more in detail below, where the emerging dislocations of the substrate help creating elementary steps facilitating the attachment of the new MCT material.

In addition, this dislocation promoted-growth exhibits, at the beginning of the growth, a lattice parameter of the MCT epilayer close to that of the substrate. This corresponds to the bright appearance of the islands in the high θ weak-beam condition of the epilayer in Fig. 2(e) and the dark appearance of these islands in the low θ weak-beam condition of the epilayer [Fig. 2(c)]. This suggests that the growth velocity is higher at these points compared with other parts of the growing epilayer. To justify this explanation, the relative growth velocity can be correlated with the final thickness of a thin film. Fig. 6(b) shows the intensity line profile of an integrated intensity map of 12 images at the high θ weak-beam condition of the epilayer. In Fig. 6(a), the white colored regions show the parts of the MCT epilayer at the very beginning of the growth with a lattice parameter close to that of the substrate. One can correlate the intensity of the matrix with these white regions. Note that the red regions are associated with the TDs emerging from the substrate. The line profile in Fig. 6(b) shows that the intensity around the islands is higher by a factor of two to four than that of the matrix. If the sample thickness is smaller than half the distance of extinction, the integrated intensity curves of kinematic and dynamic diffraction conditions are linearly proportional to the thickness (Authier, 2006). The extinction distance of the MCT epilayer in our configuration is $\Lambda = 8.6$ μm. We can correlate the relative growth velocity as a function of the diffracted intensity for the inception of the growth, which exhibits a lattice parameter different from that of most of the epilayer volume. This means that the islands grew faster with a factor of two to four compared with that of the matrix in the beginning of the growth, meaning that the growth velocity of the epilayer
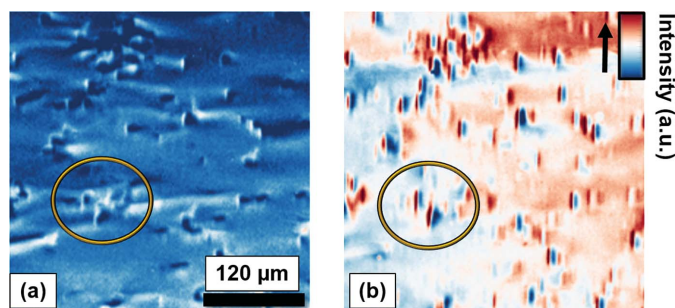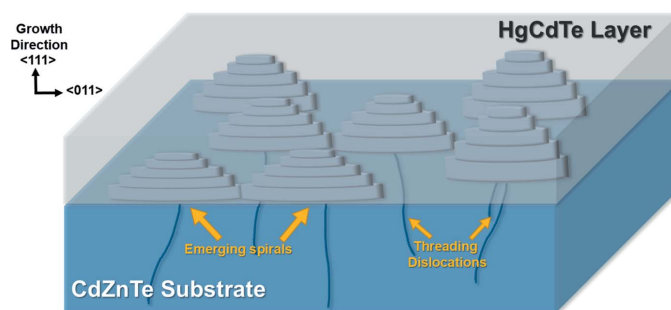
Figure 7
Schematic of the spiral growth of the MCT layer on the CZT substrate.

is higher above the emergence of the defects present on the substrate, which propagated in this way to the epilayer. Another outcome of this observation reflects on the surface topology of the MCT epilayer. The white colored regions correspond to 'pyramids' displaying a faster growth compared with zones without emerging defects from the substrate (*i.e.* blue zones). Their thickness is calculated to be ~100–200 nm by considering the separation between the pyramids (50–60 μm) and the atomic step growth observed by the AFM (~0.5 nm). However, from the AFM and interferometry results (Fig. 4) we see that the final surface topology of the MCT epilayer shows level differences ~10–20 nm. We can infer that the MCT epilayer regions without the effect of the emerging CZT dislocations, which start to grow slower in the beginning, catch up with the bright colored islands at the end of the final MCT epilayer thickness. During the growth, the lattice parameter of the MCT epilayer progressively departs from that of the substrate during further growth. This departure essentially means that the growing MCT layer changes its local composition to accommodate the strain. The departure is not uniform: the rocking curve of Fig. 2(a) displays a clear peak, indicating that the epilayer exhibits, over a substantial fraction of its volume, a given lattice parameter.

Fig. 7 illustrates the growth of the MCT epilayer suggested by our XBDI results. The initial growth becomes more sluggish when various 'pyramids' meet each other and form islands as shown in Fig. 7. Ultimately, the growth of the MCT epilayer depends on the number density and the spatial distribution of emerging dislocations from the CZT substrate. Similar growth conditions were observed for MCT and different systems such as GaAs, Ge and NaCl (Fourreau *et al.*, 2016; Möhling *et al.*, 1993; Bethge & Keller, 1974; Bauser & Strunk, 1981). Notably, screw dislocations that emerge at the surface provide spiral-growth sites meaning that growth around these dislocations occurs in a spiral manner (Quéré, 1998). The sign of these dislocations determines the right- or left-handedness of the spirals (Möhling *et al.*, 1993).

5. Conclusion

We demonstrated a monochromatic X-ray Bragg topography approach for studying the correlated defects in LPE-grown MCT epilayers on CZT substrates. We showed, using rocking

Figure 6
(a) Integrated intensity map of 12 images at the high θ weak-beam condition of the MCT layer showing the growth islands around the threading dislocations. (b) Intensity profile of the red line of the image (a). Intensity scales are the same for both images.

curve imaging, that one can study large scale (mm) distortions of the MCT epilayer originating from the substrate defects. We furthermore discussed that the TDs of the substrate emerge through the epilayer and form regions that have a faster growth velocity, partly determining the growth topology of the MCT epilayer. Our results showed that the lattice parameter of the growing epilayer in these regions are very close to that of the substrate and progressively departs from it as the growth advances, but that a substantial part of the epilayer displays a given lattice parameter. Our complementary AFM and optical interferometry results agree well with epilayer defects observed using section XBDI coupled with a tungsten block. This last method can be used to differentially determine the dislocation densities over large areas by blocking the diffraction contribution of a selected part of a material system. Thus, the applicability of this method may be extended from monolayer systems to multilayer heterostructures. We are aware that our results show indirect evidence on the growth mechanism compared with *in situ* studies or interrupted studies at different growth times. However, these experiments are difficult to realize, and can imply considering other experimental (different growth conditions to allow *in situ* observation) and physical (consequences of the growth interruption) issues. Our work contributes to the understanding of the growth mechanisms in many aspects, yet further complementary *in situ* evidence would clearly be extremely useful in order to have a full grasp of the underlying physics.

References

Authier, A. (2006). *International Tables for Crystallography*, Vol. B, *Reciprocal Space*, edited by U. Shmuelipp, pp. 626–646. Chester: International Union of Crystallography.
Ayers, J. (1994). *J. Cryst. Growth*, **135**, 71–77.
Basson, J. & Booyens, H. (1983). *Phys. Status Solidi A*, **80**, 663–668.
Bauser, E. & Strunk, H. (1981). *J. Cryst. Growth*, **51**, 362–366.
Bethge, H. & Keller, K. (1974). *J. Cryst. Growth*, **23**, 105–112.
Bowen, D. K. & Tanner, B. K. (1998). *High Resolution X-ray Diffractometry and Topography*. CRC press.
Brellier, D., Gout, E., Gaude, G., Pelenc, D., Ballet, P., Miguet, T. & Manzato, M. (2014). *J. Elec Mater.* **43**, 2901–2907.
Cockayne, D., Ray, I. & Whelan, M. (1969). *Philos. Mag.* **20**, 1265–1270.
Everson, W., Ard, C., Sepich, J., Dean, B., Neugebauer, G. & Schaake, H. (1995). *J. Electron. Mater.* **24**, 505–510.
Fourreau, Y., Pantzas, K., Patriarche, G. & Destefanis, V. (2016). *J. Elec Mater.* **45**, 4518–4523.
Frank, F. (1949). *Discuss. Faraday Soc.* **5**, 48–54.
Fung, K., Wang, N. & Sou, I. (1997). *Appl. Phys. Lett.* **71**, 1225–1227.
Hähnert, I. & Schenk, M. (1990). *J. Cryst. Growth*, **101**, 251–255.
Jakobsen, A. C., Simons, H., Ludwig, W., Yildirim, C., Leemreize, H., Porz, L., Detlefs, C. & Poulsen, H. F. (2019). *J. Appl. Cryst.* **52**, 122–132.
Köhler, R. (1994). *Appl. Phys. A*, **58**, 149–157.
Lang, A. R. (1963). *Br. J. Appl. Phys.* **14**, 904–907.
Lübbert, D., Baumbach, T., Härtwig, J., Boller, E. & Pernot, E. (2000). *Nucl. Instrum. Methods Phys. Res. B*, **160**, 521–527.
Lübbert, D., Ferrari, C., Mikulík, P., Pernot, P., Helfen, L., Verdi, N., Korytár, D. & Baumbach, T. (2005). *J. Appl. Cryst.* **38**, 91–96.
Marichev, A., Levin, R., Pushnyii, B., Gagis, G., Vasil'ev, I., Scheglov, M., Kazantsev, D. Y., Ber, B. Y., Popova, T. & Marukhina, E. (2018). *J. Phys. Conf. Ser.* **1135**, 012076.
Matthews, J. & Blakeslee, A. (1974). *J. Cryst. Growth*, **27**, 118–125.
Möhling, W., Weishart, H. & Bauser, E. (1993). *J. Cryst. Growth*, **130**, 466–474.
Pelenc, D., Merlin, J., Etcheberry, A., Ballet, P., Baudry, X., Brellier, D., Destefanis, V., Ferron, A., FougèRes, P., Giotta, D., Grangier, C., Mollard, L., Perez, A., Rochette, F., Rubaldo, L., Vaux, C., Vigneron, J. & Zanatta, J. (2014). *J. Elec. Mater.* **43**, 3004–3011.
Pelliciari, B. (1994). *Prog. Cryst. Growth Charact. Mater.* **29**, 1–39.
Quéré, Y. (1998). *Physics of Materials.* CRC Press.
Sauvage, M., Tanner, B. & Bowen, D. (1980). *Characterization of Crystal Growth Defects by X-ray Methods*, Vol. 63 of *NATO Science Series B – Physics.* New York: Springer US.
Servidori, M., Cembali, F. & Milita, S. (2001). *Appl. Phys. A*, **73**, 75–82.
Takigawa, H., Yoshikawa, M. & Maekawa, T. (1988). *J. Cryst. Growth*, **86**, 446–451.
Tanner, B. K. (2013). *X-ray Diffraction Topography: International Series in the Science of the Solid State*, Vol. 10. Elsevier.
Tran Thi, T. N., Morse, J., Caliste, D., Fernandez, B., Eon, D., Härtwig, J., Barbay, C., Mer-Calfati, C., Tranchant, N., Arnault, J. C., Lafford, T. A. & Baruchel, J. (2017). *J. Appl. Cryst.* **50**, 561–569.
Tsoutsouva, M., Oliveira, V., Camel, D., Tran Thi, T. N., Baruchel, J., Marie, B. & Lafford, T. (2014). *J. Cryst. Growth*, **401**, 397–403.
Williams, D. B. & Carter, C. B. (1996). *Transmission Electron Microscopy*, pp. 3–17. Springer.